ARL-TR-8488 ● SEP 2018

US Army Research Laboratory

Lead Zirconate Titanate (PZT) Microelectromechanical System (MEMS) HF/VHF Resonators and Filters for 50-ohm Termination

by RQ Rudy, JS Pulskamp, M Breen, JM Puder, SY Li, SS Bedair, and RG Polcawich

NOTICES

Disclaimers

The findings in this report are not to be construed as an official Department of the Army position unless so designated by other authorized documents.

Citation of manufacturer’s or trade names does not constitute an official endorsement or approval of the use thereof.

Destroy this report when it is no longer needed. Do not return it to the originator.

ARL-TR-8488 ● SEP 2018

US Army Research Laboratory

Lead Zirconate Titanate (PZT) Microelectromechanical System (MEMS) HF/VHF Resonators and Filters for 50-ohm Termination

by RQ Rudy, JS Pulskamp, SS Bedair, and RG Polcawich
Sensors and Electron Devices Directorate, ARL

M Breen and SY Li
College Qualified Leaders Program, Academy of Applied Science, Concord, NH

JM Puder
College Qualified Leaders Program, Academy of Applied Science, Concord, NH
Oak Ridge Associated Universities, Oak Ridge, TN

REPORT DOCUMENTATION PAGE

Form Approved
OMB No. 0704-0188

1. REPORT DATE *(DD-MM-YYYY)*	2. REPORT TYPE	3. DATES COVERED (From - To)
September 2018	Technical Report	June 2015–January 2018

4. TITLE AND SUBTITLE
Lead Zirconate Titanate (PZT) Microelectromechanical System (MEMS) HF/VHF Resonators and Filters for 50-ohm Termination

5a. CONTRACT NUMBER

5b. GRANT NUMBER

5c. PROGRAM ELEMENT NUMBER

6. AUTHOR(S)
RQ Rudy, JS Pulskamp, M Breen, JM Puder, SY Li, SS Bedair, and RG Polcawich

5d. PROJECT NUMBER

5e. TASK NUMBER

5f. WORK UNIT NUMBER

7. PERFORMING ORGANIZATION NAME(S) AND ADDRESS(ES)
US Army Research Laboratory
ATTN: RDRL-SER-L
2800 Powder Mill Road
Adelphi, MD 20783-1138

8. PERFORMING ORGANIZATION REPORT NUMBER
ARL-TR-8488

9. SPONSORING/MONITORING AGENCY NAME(S) AND ADDRESS(ES)

10. SPONSOR/MONITOR'S ACRONYM(S)

11. SPONSOR/MONITOR'S REPORT NUMBER(S)

12. DISTRIBUTION/AVAILABILITY STATEMENT
Approved for public release; distribution is unlimited.

13. SUPPLEMENTARY NOTES

14. ABSTRACT
This report covers lead zirconate titanate (PZT) resonators and filters in the high-frequency and very-high-frequency bands. Design of resonators for 50-ohm termination are described, resulting in resonators with insertion loss below 1 dB that are orders of magnitude smaller than similar commercial parts at this frequency. Design of monolithically integrated flexure and extension resonators with varied coupling and quality factors are presented with cross-wafer uniformity data for extensional devices.

15. SUBJECT TERMS
piezoelectric, resonator, PZT, MEMS, filter

16. SECURITY CLASSIFICATION OF:			17. LIMITATION OF ABSTRACT	18. NUMBER OF PAGES	19a. NAME OF RESPONSIBLE PERSON
a. REPORT	b. ABSTRACT	c. THIS PAGE			RQ Rudy
Unclassified	Unclassified	Unclassified	UU	33	19b. TELEPHONE NUMBER (Include area code) (301) 394-2324

Contents

List of Figures iv

List of Tables v

1. Introduction 1

2. Fabrication 2

3. Modeling and Design 4

3.1 Modeling Performance of Resonators with Parasitic Resistance 4

3.2 Design and Operation of a Disk Flexure Resonator 8

4. Experimental Results 10

4.1 Length Extension Resonators 10

4.2 Disk Flexure Resonators 17

4.3 Comparison of Monolithically Integrated Resonators 18

5. Conclusions 19

6. References 21

List of Symbols, Abbreviations, and Acronyms 25

Distribution List 26

List of Figures

Fig. 1 Comparison in size of a two-pole PZT MEMS filter atop a commercially available 70-MHz SAW filter 1

Fig. 2 Fabrication process for PZT-on-silicon resonators: a) piezoelectric stack deposition and patterning, b) gold deposition, trench etch, and passivation, c) sacrificial photoresist deposition and electrical contact bridging, and d) removal of sacrificial photoresist and XeF_2 release ... 3

Fig. 3 The mBVD model for a two-port resonator. Tether resistance, R_{ps}, can have dramatic effects on performance. 5

Fig. 4 The plotted ratio of unloaded quality factor to mechanical quality factor shows that for low motional resistance resonators, parasitic resistance can dramatically degrade the quality factor of the resonator 7

Fig. 5 Modeled S_{21} as a function of R_m and R_{ps} shows that R_{ps} has significant impact on resonator performance 7

Fig. 6 A micrograph of the arrayed disk flexure resonators. Gold is laced on the traces and electrode to reduce parasitic resistance. 9

Fig. 7 ANSYS modal analysis showing a) mode shape and b) modal stress profile. Material located at high stress points produces large coupling 10

Fig. 8 The scatter plot of measured results from a cross-wafer study highlights the increased quality factor with increasing numbers of tethers in parallel, as well as lower insertion loss with 16 tethers. Circles are individual data points, and diamonds represent the average with error bars of 1 standard deviation. 11

Fig. 9 (a) Standard resonator with high parasitic resistance in tethers. (b) Gold-laced resonator otherwise identical to (a). 12

Fig. 10 Scattering parameter ($|S_{21}|$) for the standard resonator (Fig. 9a) and gold-laced resonator (Fig. 9b) showing improvement in insertion loss (7.11 dB → 1.73 dB) unloaded circuit quality factor (735 → 2663).. 12

Fig. 11 Scattering parameter ($|S_{21}|$) for the standard resonator (Fig. 9a) and gold-laced resonator (Fig. 9b) at higher bias to decrease coupling showing improved unloaded circuit quality factor (3270 → 6220).... 13

Fig. 12 The scatter plot of measured results from a cross-wafer study shows length extension resonators with shunt impedance near 50 ohm have the lowest loss 14

Fig. 13 Measured $|S_{21}|$ response of a 10.8-MHz PZT-on-Si two-pole intermediate frequency filter 15

Fig. 14 The scatter plot of measured results from identical devices in a cross-wafer study shows a wide variation in quality factor even within a die.

The variations in $e_{31,f}$ across this wafer result in the distinct motional resistance vs. Q trend lines..... 16

Fig. 15 The 50-ohm terminated $|S_{21}|$ response has a peak of –1 dB with a bandwidth of 1.10%. The extracted coupling factor is 2.1%, and the extracted mechanical quality factor is 815 resulting in a figure of merit (FOM) of 17.2..... 17

Fig. 16 The 50-ohm terminated $|S_{21}|$ response of the disk flexure and length extension resonator are plotted atop one another showing the varied performance of the two resonators fabricated on the same die..... 19

List of Tables

Table 1 Comparison of PZT MEMS filter results with commercially available acoustic filters..... 15

Table 2 Comparison of length extension and disk flexure resonators from the same PZT-on-SOI Die..... 18

1. Introduction

While recent research in microelectromechanical system (MEMS) radio frequency (RF) resonators and filters has focused on the ultra-high-frequency band for cellular applications,[1–7] MEMS offers the potential for large gains over current commercial components in the high-frequency (HF) and very-high-frequency (VHF) bands, especially for demanding defense applications. Furthermore, the crowded and dynamic nature of the RF spectrum will require more frequency agility in the future, thereby increasing the value of integrated filter banks.[8] The lithographically defined resonance frequencies of RF-MEMS resonators enables monolithic manufacturing of filters across a broad frequency range, along with the promise of size and system integration benefits.

Piezoelectric materials are attractive for RF MEMS resonators and filters because they enable large coupling and potential direct 50-ohm termination. These qualities have allowed piezoelectric resonators to become the dominant commercial technology for narrowband filtering. Materials such as aluminum nitride (AlN) and zinc oxide (ZnO) are common choices for piezoelectric transduction due to their coupling factors and ease of fabrication. Lithium niobate (LN), a common material for surface acoustic wave (SAW) resonators, has recently been investigated as a material for MEMS resonators[9–12] due to its large material coupling factors and high phase velocity, enabling high-frequency devices with wide bandwidth. Lead zirconate titanate (PZT) offers similarly large material coupling factors,[13,14] along with large piezoelectric constants (e.g., $e_{31,f}$ of –18 C/m^2 or higher[15]) enabling high-performance actuators to be monolithically integrated with electromechanical resonators. Since the permittivity of PZT is significantly larger than AlN, ZnO, or LN, direct 50-ohm terminated resonators in the HF and VHF bands can be made small compared to commercially available filters (Fig. 1). The low phase velocity and large permittivity, however, can prevent scaling frequencies above 500 MHz.

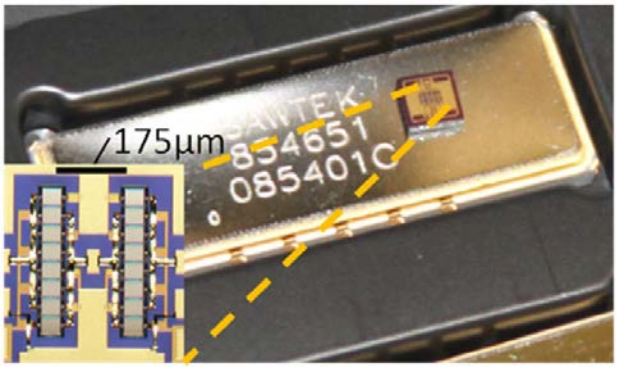

Fig. 1 Comparison in size of a two-pole PZT MEMS filter atop a commercially available 70-MHz SAW filter[13]

Because the mechanical quality factor of PZT is low, single-crystal silicon is often included in the resonator to boost the resonator mechanical quality factor, Q_m[16]; however, the added silicon degrades the effective electromechanical coupling of the resonator, k_{eff}^2, the ratio of energy transduced to the energy input. The decrease in k_{eff}^2 is counteracted by the increase in Q_m and the figure of merit, $k_{eff}^2 Q_m$, remains nearly constant across silicon thicknesses.[17] The added silicon also dramatically increases the power handling of piezoelectric resonators.[18]

While silicon reduces the coupling factor of resonators operating in extensional modes, out-of-plane flexure modes can be enhanced by adding silicon to the resonator. Research in piezoelectric MEMS resonators initially focused on flexural resonators, specifically beam flexure modes.[19] These designs were abandoned in favor of length extensional resonators because the mechanical boundary conditions in the flexural beams introduced significant nonlinearities due to spring stiffening.[20] In contrast, disk flexure resonators[21], which are tethered along a nodal diameter, do not suffer from the spring stiffening effects. These disk flexure resonators have demonstrated coupling factors quadruple that of length extension resonators on the same die and with lower loss.[22] This increase in coupling factor is enabled by the added silicon and the fact that the mode transduces significant energy using both the e_{31} and e_{32} piezoelectric constants. These modes perform well at lower frequencies; however, due to unfavorable scaling properties, they are likely limited to below 100 MHz.[23] For these reasons, PZT-based disk flexure modes are of interest for HF and VHF electromechanical MEMS resonators and filters.

This report details PZT-based MEMS resonators using extensional and flexural modes designed for direct 50-ohm termination. Important considerations for the 50-ohm terminated design will be discussed, such as the importance of parasitic resistance and optimal sizing of shunt reactance. This report is organized in five sections. Following this introduction is a description of the microfabrication processes used for these resonators and filters. Section 3 contains a discussion of modeling and design of PZT resonators including a detailed treatment of parasitic resistance and sizing of shunt reactance. Results and discussion are contained in Section 4, highlighted by the monolithic integration of low-loss resonators with either high coupling or high quality factor. Section 5 includes concluding remarks.

2. Fabrication

The resonators are fabricated in a PZT-on-SOI (silicon-on-insulator) process outlined briefly below and in Fig. 2. A more detailed treatment of the entire fabrication process can be found in Pulskamp et al.[21]

The process starts by depositing and patterning the active material and electrodes, Fig. 2a. To begin the deposition, a 200-nm thermal silicon dioxide layer is grown on a 150-mm-diameter SOI wafer with a 10-µm-thick silicon device layer. Titanium is sputtered and oxidized to create a 35-nm-thick templating layer of textured TiO_2 for orienting the subsequently sputtered 100-nm platinum bottom electrode.[24] This oriented platinum electrode enables (001) oriented lead PZT with a Zr/Ti ratio of 52/48, which is deposited via chemical solution deposition.[25] The top electrode is sputtered platinum with a thickness of 50 nm. The first step in patterning the stack is to etch the top electrode, which is performed by Ar ion milling. With the top electrode defined, the rest of the actuator stack can be patterned by another Ar ion mill, down to the silicon dioxide residing on top of the device Si layer.

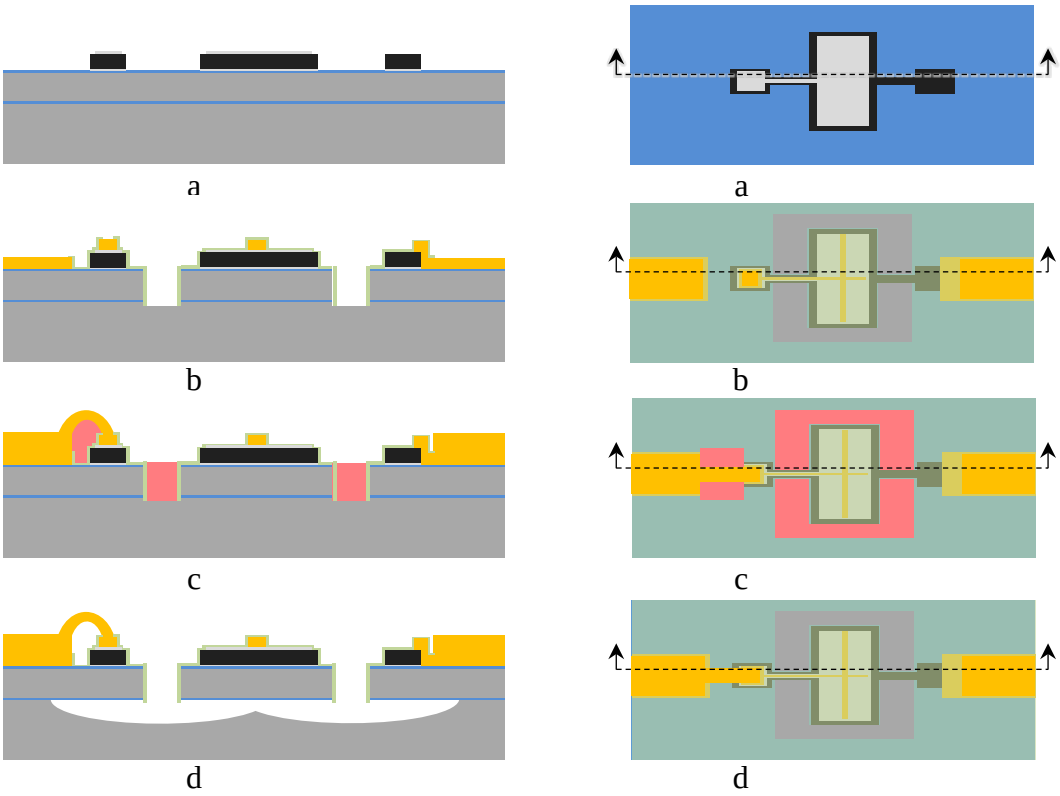

Fig. 2 Fabrication process for PZT-on-silicon resonators: a) piezoelectric stack deposition and patterning, b) gold deposition, trench etch, and passivation, c) sacrificial photoresist deposition and electrical contact bridging, and d) removal of sacrificial photoresist and XeF_2 release

With the transducers defined, electrical contacts can be deposited, the resonator body defined, and a passivation layer deposited and patterned (Fig. 2b). To form probe pads and electrical traces, Au/Pt/Cr (730 nm/20 nm/20 nm) are evaporated and patterned via lift-off, referred to as metal 1. The resonator body can be defined,

electrically connected to the probe pads, and released. To define the resonator body, a deep reactive ion etch of the silicon and a reactive ion etch of the buried oxide layer are performed, forming a trench extending into the handle wafer. A conformal layer of 25-nm HfO_2 capped 50-nm Al_2O_3 is deposited via atomic layer deposition (ALD) in a sequence of three deposition and anneal (at 500 °C in flowing O_2) procedures. This ALD layer acts as a passivation layer for the device silicon layer during the subsequent release etch in XeF_2. A reactive ion etch is performed to pattern the bottom of the trench and open access to metal 1.

With the electrical interconnects deposited and the resonator body defined, gold air bridges can be deposited with the aid of sacrificial photoresist (Fig. 2c). To reduce large step heights across the wafer and enable photoresist processing for the remainder of fabrication, the deep trench is filled with a sacrificial photoresist. A second sacrificial photoresist is patterned, upon which a 2-μm-thick gold layer is deposited and patterned with lift-off. This gold bridges from the metal 1 probe pads to the metal 1 layer on the top electrode of the transducer, eliminating the probe pad parasitic capacitance. With the entire structure defined, the sacrificial photoresist is then removed in an oxygen plasma, and the resonator is released using an isotropic XeF_2 etch (Fig. 2d).

3. Modeling and Design

This modeling and design section discusses electrical parasitic resistance and its effect on quality factor and insertion loss. Following this is a description of the design and operating principles of a novel disk flexure resonator that has exhibited lower loss than traditional length extension designs.

3.1 Modeling Performance of Resonators with Parasitic Resistance

Parasitic resistance in the top electrode can have dramatic effects on device performance, especially in low motional resistance resonators. Despite its importance, there are complex tradeoffs in material choice, layer thicknesses, and design, which motivate the following analysis. Much of this tradeoff arises from the coupling of the electrical and mechanical domains. For example, thin electrodes would be mechanically ideal; however, thin electrodes will produce large electrical parasitic resistance. Additionally, electrode materials that produce the best piezoelectric film properties can also result in larger electrical trace resistance. Large degradation in the insertion loss and quality factor of the two-port network suggest that these parasitic resistances should be considered in the design of resonators, and not removed with de-embedding or neglected.

To properly model the performance of the electromechanical resonator and the effects of the parasitic resistance in the tethers, the modified Butterworth Van Dyke (mBVD) model[26] may be used. This model adds resistance in series with the standard Butterworth Van Dyke (BVD) pi network model. Figure 3 shows the two-port mBVD model, where the equivalent motional elements, C_m, L_m, and R_m, are highlighted in blue. The parasitic resistance in the tethers is represented by R_{ps} and the shunt capacitors, C_s, represent the capacitance between signal and ground electrodes through the piezoelectric material at input and output ports. The bottom electrode resistance and capacitor loss are represented by R_b in the diagram.

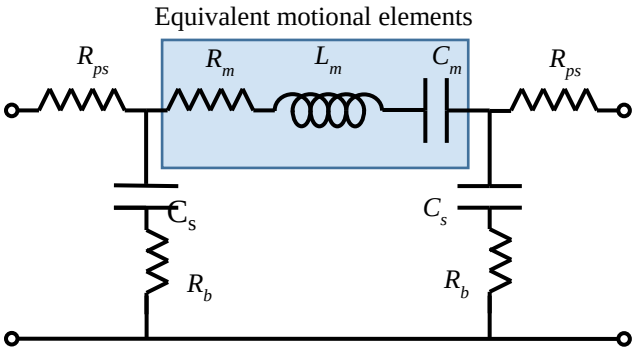

Fig. 3 The mBVD model for a two-port resonator. Tether resistance, R_{ps}, can have dramatic effects on performance.

To evaluate the effects of tether resistance on system performance, it is helpful to look at the effect tether resistance has on the forward scattering parameter, S_{21}. This can be derived analytically by cascading the ABCD matrices for the individual elements and transforming the ABCD matrix of the system into scattering parameters based on the load impedance. The magnitude of S_{21} is described in Eqs. 1 and 2.

$$|S_{21}| = \left| \frac{2}{2+\frac{Z_M}{Z_L}+\frac{2Z_L}{Z_S}+\frac{2Z_M}{Z_S}+\frac{Z_L Z_M}{{Z_S}^2}+R_{PS}\beta} \right| . \quad (1)$$

$$\beta = \frac{4Z_S+2Z_M}{{Z_S}^2} + \frac{2R_{PS}Z_S+Z_M R_{PS}+2Z_M Z_S+2{Z_S}^2}{Z_L {Z_S}^2} . \quad (2)$$

Here, the impedance of the load is Z_L, the impedance of the motional elements (motional resistance, inductance, and capacitance) is Z_M, the impedance of a shunt arm is Z_S, and the parasitic resistance from the tethers is R_{PS}. When the parasitic tether resistance is low, β does not have a significant effect on the resonator $|S_{21}|$

performance. When the tether resistance is on the order of Z_L, Z_M, or Z_S, however, there can be a significant degradation in performance due to the $R_{PS}\beta$ term in Eq. 1 as shown in the following analysis. Additionally, properly sizing the resonator for the termination is also important. If the resonator is oversized, the larger capacitance can shunt signal to ground; however, if the resonator is undersized, the motional resistance becomes large, reducing the transmission. The terms Z_l and Z_s in Eq. 2 account for this effect. In either case, mismatch also causes signal reflection.

These parasitic resistances are especially important for low R_m resonators because they can significantly affect the extracted quality factor. The quality factor of the resonator is a ratio of energy stored to energy dissipated and is an important parameter that controls the insertion loss and roll-off in filters. There are several distinct quality factors that are relevant to understanding the influence of parasitic resistance on resonator performance. The loaded quality factor, Q_L, is related to the bandwidth of the forward gain scattering parameter response, $|S_{21}|$, and accounts for the loading effect of the source and load impedances on the device response. The unloaded quality factor of the circuit, $Q_{UL,c}$,[27] excludes the loading effect of the termination impedance on the resonator and is a function of Q_L and the $|S_{21}|$ at the resonance frequency, as shown in Eq. 3. The $Q_{UL,c}$ is the traditionally reported unloaded quality factor for electromagnetic RF resonators.[27]

$$Q_{UL,c} = \frac{Q_L}{1-|S_{21}(f_0)|}. \tag{3}$$

The mechanical quality factor, Q_m, is the quality factor of the mechanical components of the resonator. Parasitic resistance, which does not affect Q_m, can have a significant effect on the extracted $Q_{UL,c}$ by loading the resonator and reducing $Q_{UL,c}$ far below Q_m as shown in Fig. 4. The plot shows the ratio of $Q_{UL,c}$ to Q_m as R_m and R_{ps} are varied (all other mBVD parameters are kept constant). For low R_m devices (<20 ohm), the addition of small R_{ps} can produce large changes in the $Q_{UL,c}$ to Q_m ratio. For example, a resonator with R_m of 7 ohm and R_{ps} of just 3 ohm would have an unloaded quality factor 30% lower than the mechanical quality factor.

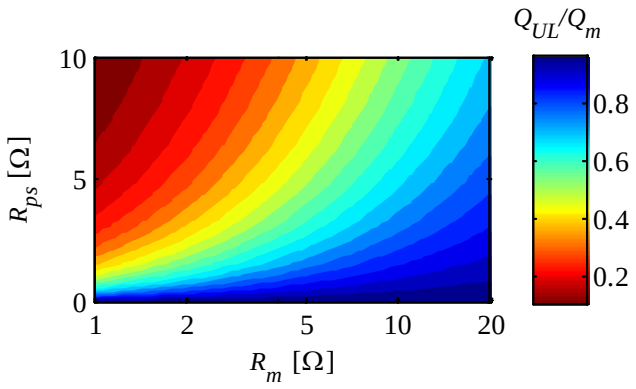

Fig. 4 The plotted ratio of unloaded quality factor to mechanical quality factor shows that for low motional resistance resonators, parasitic resistance can dramatically degrade the quality factor of the resonator

While the effects of parasitic tether resistance have been described here for low R_m resonators, these effects can be important for higher motional impedance devices as well. Figure 5 shows the simulated, 50-ohm terminated insertion loss in decibels of resonators with various series parasitic resistances over a range of motional resistances. The loss can increase significantly even for high impedance resonators.

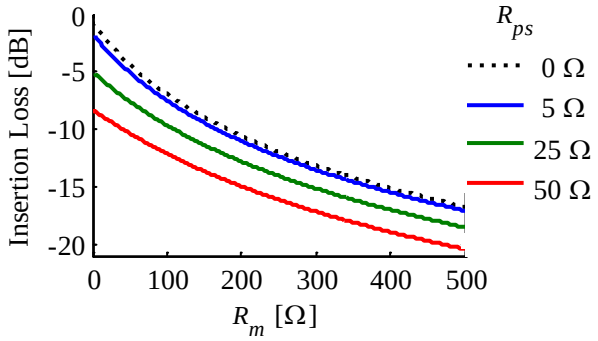

Fig. 5 Modeled S_{21} as a function of R_m and R_{ps} shows that R_{ps} has significant impact on resonator performance[32]

Parasitic resistance can be especially problematic when feature sizes decrease, especially for resonators at frequencies above 500 MHz. At these frequencies, interdigitated transducer electrodes (not just routing traces) can have non-negligible resistance, and this resistance can degrade performance similar to the effect of tether resistance described previously. Since adding more metal to the transducer electrodes on the resonator decreases coupling and mechanical quality factor, there is a necessary trade-off between the electrode resistance and resonator figure of merit for resonators at higher frequency.

3.2 Design and Operation of a Disk Flexure Resonator

While length and width extension modes are most commonly exploited in MEMS resonators, disk flexure resonators provide several benefits, such as lower loss and higher coupling. These disk flexure modes differ from the beam flexure modes investigated in the 1990s and 2000s[19] in that the tether to the substrate does not clamp the structure. Furthermore, because the mode strains in both x- and y-directions, there is a coupling enhancement from accessing both the e_{31} and e_{32} piezoelectric constants, enabling larger coupling from flexure modes than from length extension modes in PZT-on-silicon resonators. This enhanced coupling has been demonstrated recently by Cassella et al. utilizing Lamé modes to access the e_{31} and e_{33} piezoelectric constants,[28] as well as Puder et al. utilizing a flexural beam mode by accessing the e_{31} and e_{32} piezoelectric constants.[29] In length extension resonators, the effective resonator electromechanical coupling factor, k_{eff}^2, generally decreases with increased silicon thickness because the additional silicon stiffens the structure but does not contribute to the piezoelectric response. In contrast, for disc flexure modes there exists an optimal silicon thickness for device performance. In a pure PZT resonator, the mid-plane of the piezo is collinear with the neutral axis, so no bending moment exists, and there is no coupling due to flexure. If silicon is very thick, most of the mechanical energy will reside in the silicon, and the coupling approaches zero. Between these extremes, there exists a silicon thickness that provides optimal coupling for flexural modes; however, exploring this optimization space is beyond the scope of this work. The HF and VHF bands are ideal for flexural-mode MEMS resonators where the mode is not distorted by shear effects, but the resonators are still quite small. Ultimately, these flexure modes, which are not often used in MEMS resonators, can be used to create 50-ohm terminated low-loss wideband resonators at HF and VHF frequencies.

A micrograph of an example disk resonator is shown in Fig. 6, where identical disk resonators are arrayed in parallel to reduce the motional resistance and to increase the shunt capacitance of the resonator array to match the 50-ohm termination and optimize the $|S_{21}|$ response. The cutout of Fig. 6 shows a zoomed image of an individual resonator in the array highlighting the materials and device features. On each disk, gold lacing is used to reduce the parasitic resistance of the platinum traces and electrodes, which can significantly degrade performance of low motional resistance resonators as described previously.

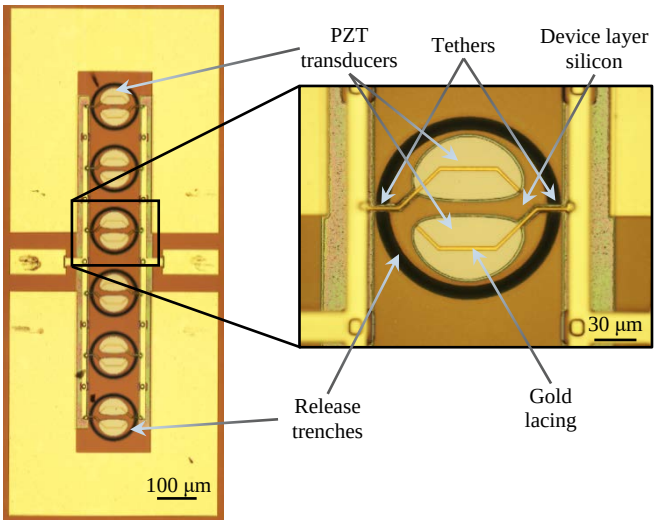

Fig. 6 A micrograph of the arrayed disk flexure resonators. Gold is laced on the traces and electrode to reduce parasitic resistance.[22]

The resonator operates in a disk flexural vibration mode, B_{11}, with a nodal diameter aligned with the tethers and a nodal circle. The modal displacement simulated in ANSYS is shown in Fig. 7a. The resonance frequency of this mode is a function of the material stack and is inversely proportional to the radius squared.[30] This square frequency relationship complicates scaling to very high frequencies because the mode shape is distorted when the aspect ratio of the disk inhibits plate-like behavior. While frequency scaling by reducing the radius can be problematic, higher frequencies can be accessed by designing the devices for higher-order modes.[31]

To excite these flexural vibration modes in the resonator, the piezoelectric material contracts and creates bending stresses in the resonator material stack, so increasing the distance the PZT is offset from the neutral plane of the disk can increase the bending stress. The PZT at each port couples electrical energy into mechanical vibration, and vice versa. The electrode pattern was designed for optimal coupling according to the procedure in Pulskamp et al.[21] by placing the electrodes where the modal stresses, shown in Fig. 7b, are largest. By limiting the area covered by the electrodes, the coupling is optimized while the proper shunt capacitance is then achieved by arraying the six individual resonators in parallel.

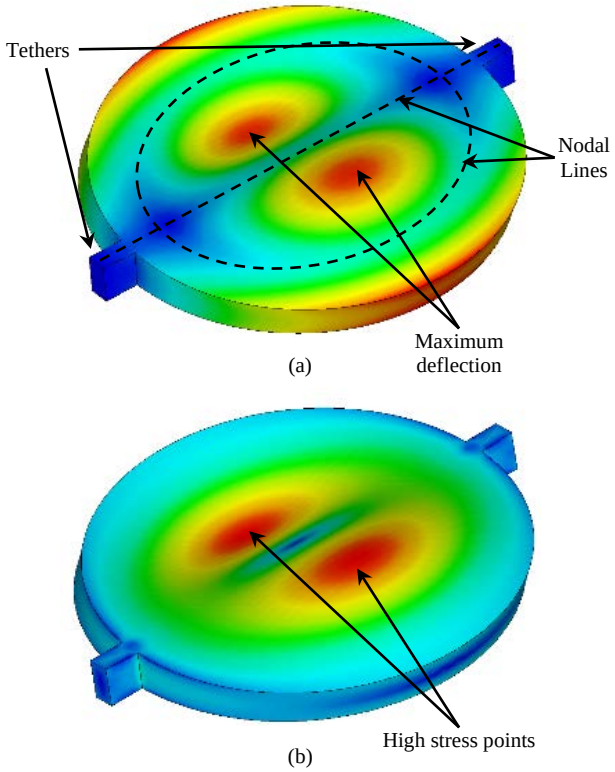

Fig. 7 ANSYS modal analysis showing a) mode shape and b) modal stress profile. Material located at high stress points produces large coupling.

4. Experimental Results

The results in this section are separated into length extension resonators, disk flexure resonators, and a comparison of these resonators monolithically integrated.

4.1 Length Extension Resonators

To demonstrate that parasitic tether resistance can have a significant effect on resonator performance, a number of resonators were fabricated with 8, 12, or 16 tethers utilizing the fourth, sixth, and eighth length extension overtone, respectively. These tethers mechanically support the resonator at nodal points but also contain the electrical traces connecting the waveguide to the top and bottom electrode on the resonator body. The 50-nm-thick top platinum electrode layer is used to form these electrical traces, so they are quite resistive (~40 ohm). Because the resistances are arrayed in parallel and only every other tether connects to the signal line of a port, each port of the eight-tether resonator sees 20-ohm parasitic resistance in the signal path. Likewise, the 12 and 16 tether resonators see 15-ohm and 10-ohm parasitic resistances in the signal path. Figure 8 shows the quality

factor and insertion loss from a number of resonators with 8, 12, or 16 tethers that are designed to have the same shunt capacitance and frequency.

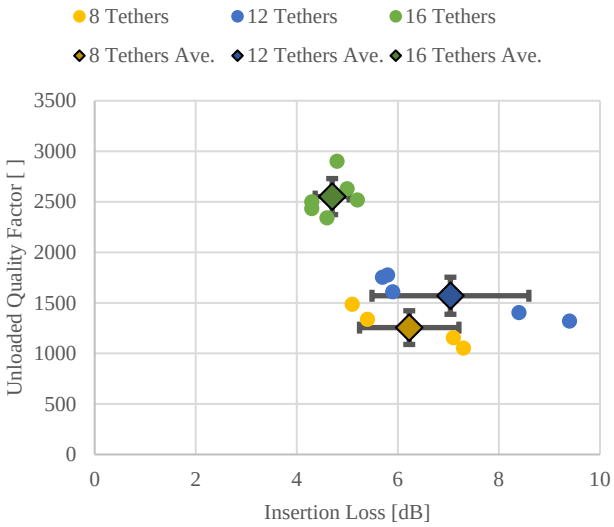

Fig. 8 The scatter plot of measured results from a cross-wafer study highlights the increased quality factor with increasing numbers of tethers in parallel, as well as lower insertion loss with 16 tethers. Circles are individual data points, and diamonds represent the average with error bars of 1 standard deviation.

The plot in Fig. 8 shows that decreasing the parasitic resistance can significantly increase the unloaded quality factor as described in Section 3. While there is wide variation in loss for the 8 and 12 tether devices, both are significantly worse than the 16 tether devices. This highlights the important role parasitic resistance can have in determining resonator performance.

To mitigate the effect of parasitic resistance on quality factor and loss, gold was laced on a resonator to reduce the parasitic resistance due to the top electrode. Figure 9a and b show micrographs of the standard resonator and the gold-laced resonator, respectively. The gold-laced resonator in Fig. 9b showed significant improvement in performance compared to the standard resonator in Fig. 9a. Specifically, the gold-lacing reduced the 50-ohm terminated insertion loss from 7.11 dB to 1.73 dB and improved the unloaded quality factor of the resonator circuit, $Q_{UL,c}$, from 735 to 2663. Figure 10 shows the $|S_{21}|$ response of the two resonators, where the improvement in insertion loss is readily apparent. The quality factor improvement is not as obvious because the lower loss resonator is loaded more by the termination. It is important to note that the gold-laced resonator has nearly identical coupling, k_{eff}^2, and a lower Q_m due to the added low-Q gold. Accordingly, while the resonator performance (insertion loss, unloaded quality factor, etc.) has been improved, the resonator figure of merit, $k_{eff}^2 Q_m$, is actually

lower for the gold-laced resonator (22.1 vs. 14.4). The frequency offset between the resonators is attributed to the added mass of the gold on the structure.

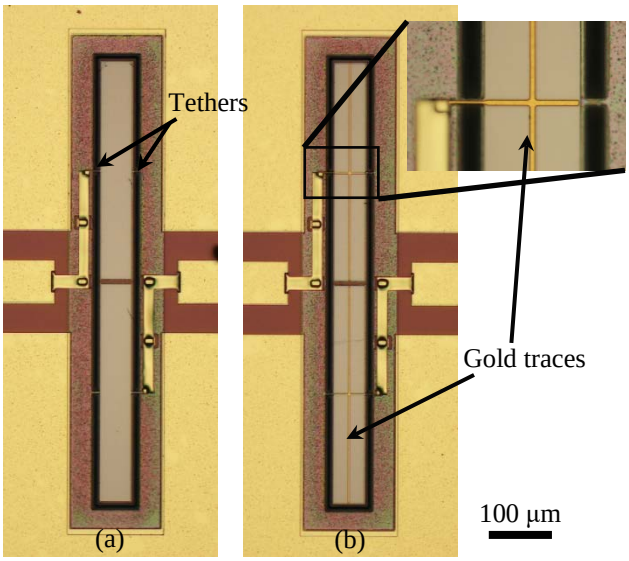

Fig. 9 (a) Standard resonator with high parasitic resistance in tethers. (b) Gold-laced resonator otherwise identical to (a).[32]

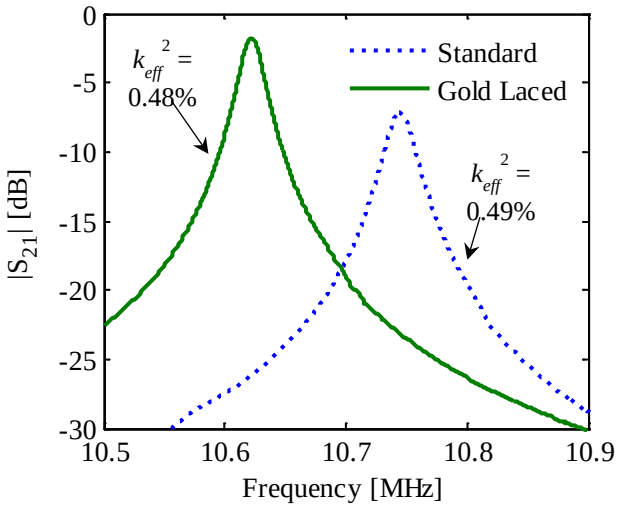

Fig. 10 Scattering parameter ($|S_{21}|$) for the standard resonator (Fig. 9a) and gold-laced resonator (Fig. 9b) showing improvement in insertion loss (7.11 dB → 1.73 dB) unloaded circuit quality factor (735 → 2663).[32]

On a different gold-laced resonator, an unloaded circuit quality factor of 6220 and 50-ohm terminated insertion loss of 4.9 dB was demonstrated when the resonator was operated at a high-bias field to limit ferroelectric domain wall motion and reduce mechanical loss. The $|S_{21}|$ response of this high-Q resonator and its companion unlaced resonator (insertion loss = 9.5 dB, $Q_{UL,c}$ = 3270) is plotted in

Fig. 11. It is again important to stress that this improvement in measured $Q_{UL,c}$ is not due in any way to the mechanical or electromechanical response of the resonator but merely the difference in parasitic electrical resistance in each of the devices.

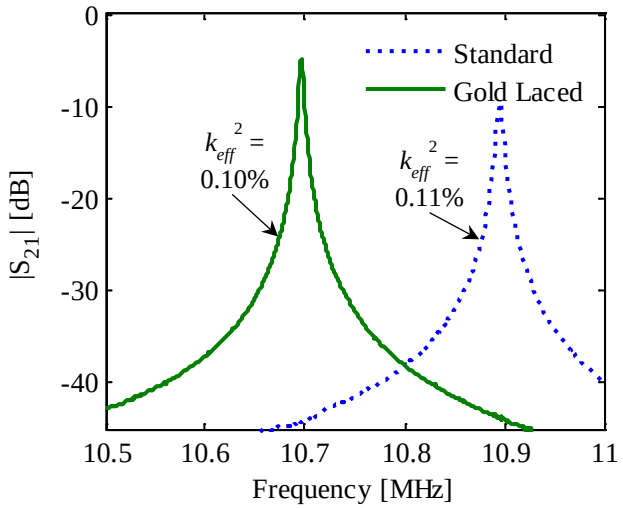

Fig. 11 Scattering parameter ($|S_{21}|$) for the standard resonator (Fig. 9a) and gold-laced resonator (Fig. 9b) at higher bias to decrease coupling showing improved unloaded circuit quality factor (3270 → 6220)[32]

While parasitic resistance is important in resonator design, optimal designing for direct 50-ohm termination is also important, especially for reducing reflection. One advantage of PZT as a piezoelectric transduction material in HF and VHF resonators is the compact size of direct 50-ohm terminated designs without the need for matching, primarily due to the large permittivity of the PZT. Changing the width of resonators (where width is orthogonal to the direction of wave propagation) modifies the shunt impedance, which for this case is optimally near 50 ohm. To demonstrate this effect, a number of two-port resonators with varied width were fabricated and characterized. The insertion loss and shunt impedance for each width are plotted in Fig. 12.

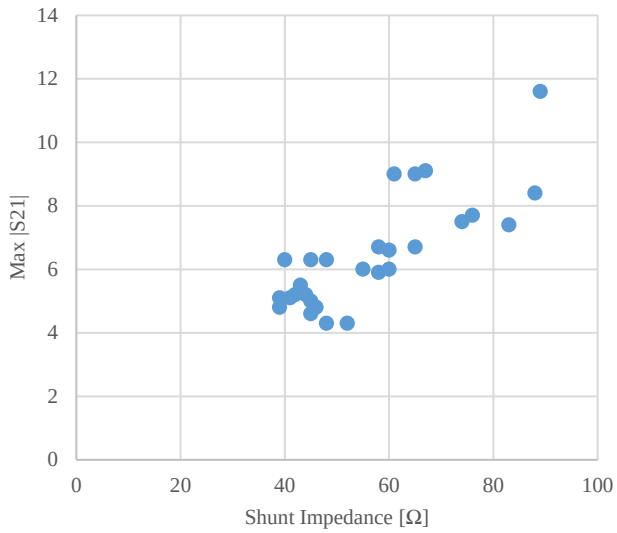

Fig. 12 The scatter plot of measured results from a cross-wafer study shows length extension resonators with shunt impedance near 50 ohm have the lowest loss

The trend of insertion loss as a function of shunt impedance in Fig. 12 highlights the importance of optimal design. From this plot it is clear that devices with shunt impedance near 50 ohm show the lowest loss, which is attributed to the close match to the optimal shunt impedance of each port. This is important to note because motional resistance, which also contributes to insertion loss, decreases with lower shunt impedance. As the shunt impedance decreases below 50 ohm, however, the benefit of lower motional resistance is countered by the reactance mismatch of shunt impedance.

While these individual resonators can achieve low insertion loss, the out-of-band rejection can be relatively poor, largely due to spurious resonance modes. In order to improve rejection, these resonators can be arranged in a self-coupled topology.[33] Figure 13 displays the wideband measured $|S_{21}|$ response of a PZT-on-silicon self-coupled two-pole filter at 10.8 MHz.

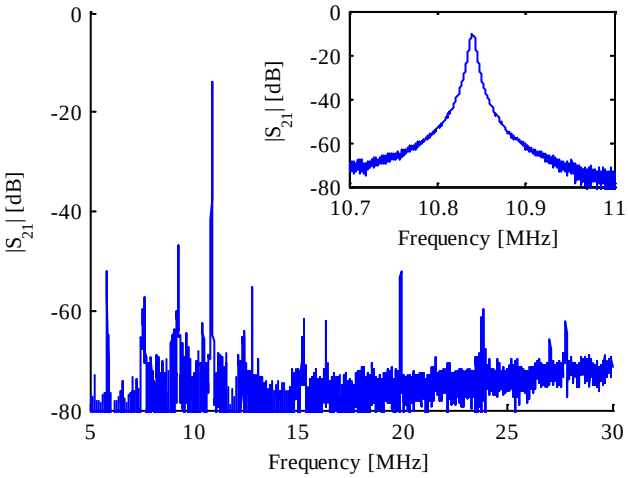

Fig. 13 Measured $|S_{21}|$ response of a 10.8-MHz PZT-on-Si two-pole intermediate frequency filter[13]

This plot shows the wideband response with multiple out-of-band spurs with amplitudes smaller than –50 dB. It can be seen from the narrow sweep plot that the roll-off of 2.1 dB/kHz is relatively steep and the ultimate attenuation is 60 dB. In order to compare this filter to commercial components, Table 1 lists the performance of this filter as well as similar low-frequency commercially available acoustic filters, including monolithic quartz, SAW, and ceramic technologies.[34]

Table 1 Comparison of PZT MEMS filter results with commercially available acoustic filters[34]

Filter technology	No. poles	Frequency (MHz)	Bandwidth (%)	Insertion loss (dB)	Roll-off (dB/kHz)	Ultimate attenuation (dB) (±1.5 MHz)	Term. imp. (Ω)	Component size (mm^3)	Max. input power (dBm)
This work	2	10.8	0.04	9	2.1	60	50	5.2	13
Monolithic Quartz	2	10.7	0.07	1.5	1.1	35	1800	587.3	–10
Ceramic	…	10.7	1.03	9	0.2	30	330	339.0	…
SAW	…	43.8	6.86	14.8	0.04	42	2000	826.1	27

The PZT-on-silicon filter without external impedance matching performs well compared to commercial technologies, though component size is where this work provides the largest value. Quartz has lower loss, and because of the lower loss, the bandwidth is increased because of external loading. SAW exhibits higher power handling; however, this is at a higher frequency, which usually enables better power handling. The performance listed for the commercially available filters is for the case of external impedance matching while the PZT MEMS filter is directly terminated to 50 ohms. The component size listed accounts for the size of the required discrete matching elements for the commercially available filters and the input and output bias tees for the PZT MEMS filter (assumes 0402 size

components). While the performance of the PZT-on-silicon two-pole intermediate frequency filter meets the requirements of the intended application at a dramatically smaller size compared to commercial parts, the resonators in this filter exhibited significant parasitic resistance, degrading the quality factor and insertion loss of the device as described in Section 3. Since the two resonators are cascaded, the parasitic resistance of each resonator degrades the overall filter performance. It is therefore expected that when this resistance is mitigated, insertion loss will drop to 3.5 dB or less and roll-off will increase to 2.8 dB/kHz.

While the performance of these PZT MEMS resonators and filters compares well with commercial parts, especially if parasitic resistance can be mitigated, significant variation in performance can be observed from device to device and die to die. Figure 14 plots the extracted motional resistance and mechanical quality factor for identical devices on the same die for four different die on a single wafer.

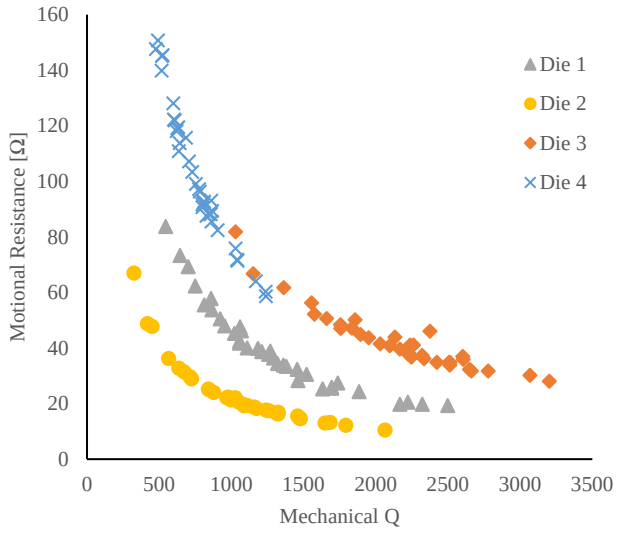

Fig. 14 The scatter plot of measured results from identical devices in a cross-wafer study shows a wide variation in quality factor even within a die. The variations in $e_{31,f}$ across this wafer result in the distinct motional resistance vs. Q trend lines.

From this plot, it is clear that there can be a wide variation in mechanical quality factor on the same die. The source of this variation is not easily identifiable, especially since understanding and modeling sources of loss in resonators is a subject of much ongoing research.[35,36] Another important observation is that there is significant die-to-die variability in the motional resistance trend curves. It has been shown that for length extensional resonators, the motional resistance is inversely proportional to the mechanical quality factor and the square of the piezoelectric stress constant, e_{31}, assuming identical material and geometric properties.[18] Because the resonators are designed identically, the different trend

curves represent different piezoelectric stress constants across the wafer. While the spread in e_{31} within each die appears quite low, the spread across the wafer could prove problematic. More must be done to understand and eliminate this cross-wafer nonuniformity.

4.2 Disk Flexure Resonators

Disk flexure resonators, which can exhibit benefits over length extension resonators, were fabricated and tested in air using a 50-ohm terminated network analyzer. The S_{21} response is plotted in Fig. 15 showing a peak $|S_{21}|$ of –1 dB. The motional properties of the device were extracted and result in a motional resistance of 9 ohm, an effective coupling factor, k_{eff}^2, of 2.1%, and a mechanical quality factor, Q_m, of 815.

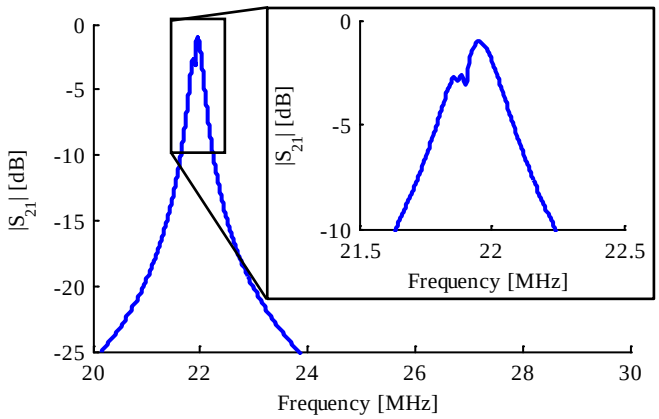

Fig. 15 The 50-ohm terminated $|S_{21}|$ response has a peak of –1 dB with a bandwidth of 1.10%. The extracted coupling factor is 2.1%, and the extracted mechanical quality factor is 815 resulting in a figure of merit (FOM) of 17.2.[22]

Frequency splitting, which can be observed in the zoomed plot in Fig. 15, is attributed to the offset in frequencies of some of the resonators in the array, and is currently being investigated further. Due to this frequency splitting in the array the bandwidth is slightly elevated, as is k_{eff}^2, which is determined from fitting the motional and shunt capacitances. The resonator figure of merit (FOM), $k_{eff}^2 * Q_m$, for this device is 16.9. A similar disk flexure resonator in PZT on 4-µm-thick SOI exhibited a coupling factor over 5%, though with a lower quality factor.

Power handing was measured on a similar disk flexure resonator, and 1-dB compression was not observed up to the +15 dBm supply limit on the network analyzer. Very little deviation in behavior is observed up to +5 dBm. This large power handling is in part related to the additional material from the silicon device layer. With more mass, the resonator can store more energy before nonlinear effects

dominate the response. All other measurements recorded in this report were taken at –15 dBm sourced from the network analyzer.

4.3 Comparison of Monolithically Integrated Resonators

These disk flexure resonators were monolithically integrated with the previously described narrow, low-loss length extension resonators. Table 2 compares an 11-MHz length extension and a 22-MHz disk flexure resonator from the same wafer die. The disk resonator exhibits 4 times higher coupling factor compared to the length extension device, while the length extension resonator has a 3.75 times higher quality factor and 5.5 times narrower bandwidth. Figure 16 shows these devices plotted together, normalized by center frequency, highlighting the significant difference in bandwidth and roll-off of the two resonators, while maintaining similar insertion loss. The cutout of Fig. 16 is a micrograph of the two resonators directly adjacent to one another on the wafer die.

These disk flexure and length extension resonators fabricated on the same die and were not subjected to specialized release etches. In this case, on the same die one can trade coupling for quality factor while maintaining insertion loss, FOM, and motional resistance. Beyond this discrete design-based flexibility, the responses of each of these resonators are tunable due to the ferroelectric nature of the PZT active material, further enabling RF system agility and flexibility.

Table 2 Comparison of length extension and disk flexure resonators from the same PZT-on-SOI Die[22]

Performance metric	Length extension[32]	Disk flexure[22]
Intrinsic loss	1.58 dB	0.92 dB
Effective resonator coupling factor (k_{eff}^2)	0.48%	2.09%
Mechanical quality factor (Q_m)	3000	815
Resonator figure of merit ($k_{eff}^2 \cdot Q_m$)	14.4	16.9
3-dB bandwidth %	0.20%	1.10%
Motional resistance	16 ohm	9 ohm

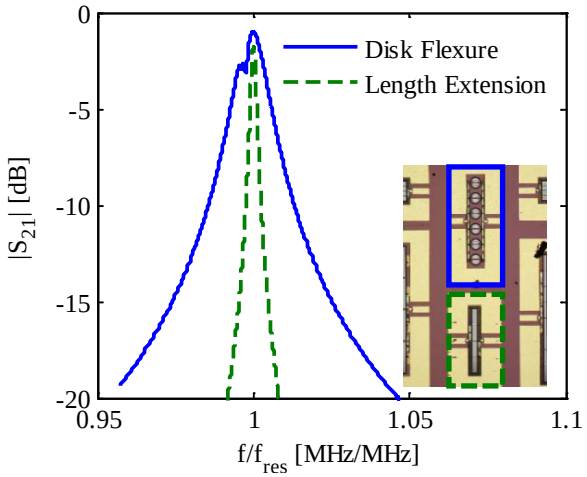

Fig. 16 The 50-ohm terminated $|S_{21}|$ response of the disk flexure and length extension resonator are plotted atop one another showing the varied performance of the two resonators fabricated on the same die[22]

5. Conclusions

This report highlights recent work in developing PZT-based resonators and RF filters at HF and VHF frequencies. Of note is the importance of parasitic resistance in resonators, proper sizing of shunt capacitances, and high-performance flexural mode resonators monolithically integrated with length extension resonators.

Parasitic resistance is an important parameter in resonators and has great significance when examining low motional impedance resonators. Resonators presented in this report showed dramatic improvement in insertion loss (IL 7.11 dB→1.73 dB) and quality factor ($Q_{UL,c}$ 735→2663), simply due to reducing parasitic resistance. Reducing parasitic resistance may substantially improve insertion loss compared to improving resonator FOM depending on the resonator. As higher-coupling materials, such as PZT and LN, become more prominent, and high-coupling modes, such as Lamé and flexure, continue to be explored, the parasitic resistance of electromechanical MEMS resonators will become more important. Because it can have such a significant effect on performance, these values should be extracted and reported, not neglected or calibrated out.

Flexure modes, which are not commonly explored in MEMS, have potential to offer large coupling factors with reasonable quality factors. These disk flexure two-port resonators exhibited lower loss than length extension resonators on the same wafer. Because flexure modes can exhibit large coupling and lower loss than the widely used length extension mode, additional exploration of these modes is warranted.

Even if not for use as intended resonant modes, then certainly for reduction of spurious modes, which become important when material coupling factors are large.

Both disk flexure and length extension resonators can be fabricated together, enabling high quality factor resonators and high coupling factor resonators monolithically integrated. Because the resonance frequencies of these filters are defined by lateral dimensions, this monolithic integration can enable monolithic filter banks that span a range of frequencies as well as provide varied coupling factor and quality factor according to design. This flexibility could be especially useful for future communication systems as more filters are required to fit in smaller volumes.

6. References

1. Piazza G, Stephanou PJ, Pisano AP. One and two port piezoelectric higher order contour-mode MEMS resonators for mechanical signal processing. Solid-State Electron. 2007;51(11–12):1596–1608.

2. Cassella C, Hui Y, Qian Z, Hummel G, Rinaldi M. Aluminum nitride cross-sectional lamé mode resonators. Journal of Microelectromechanical Systems. 2016 April;25(2):275–285.

3. Gong S, Piazza G. Design and analysis of lithium–niobate-based high electromechanical coupling RF-MEMS resonators for wideband filtering. IEEE Transactions on Microwave Theory and Techniques. 2013 Jan;61(1):403–414.

4. Olsson RH, Washburn CM, Stevens JE, Tuck MR, Nordquist CD. VHF and UHF mechanically coupled aluminum nitride MEMS filters. IEEE International Frequency Control Symposium; 2008; Honolulu, HI. p. 634–639.

5. Popa LC, Weinstein D. Switchable piezoelectric transduction in AlGaN/GaN MEMS resonators. 2013 Transducers & Eurosensors XXVII: The 17th International Conference on Solid-State Sensors, Actuators and Microsystems (TRANSDUCERS & EUROSENSORS XXVII); 2013; Barcelona, Spain. p. 2461–2464.

6. Chandrahalim H, Weinstein D, Cheow LF, Bhave SA. Channel-select micromechanical filters using high-K dielectrically transduced MEMS resonators. 19th IEEE International Conference on Micro Electro Mechanical Systems; 2006; Istanbul, Turkey. p. 894–897.

7. Pourkamali S, Ho GK, Ayazi F. Low-impedance VHF and UHF capacitive silicon bulk acoustic wave resonators—part I: concept and fabrication. IEEE Transactions on Electron Devices. 2007 Aug;54(8):2017–2023.

8. Aigner R. Tunable filters? Reality check foreseeable trends in system architecture for tunable RF filters. IEEE Microwave Magazine. 2015 Aug;16(7):82–88.

9. Kadota M, Ogami T, Yamamoto K, Tochishita H, Negoro Y. High-frequency lamb wave device composed of MEMS structure using $LiNbO_3$ thin film and air gap. IEEE Transactions on Ultrasonics, Ferroelectrics, and Frequency Control. 2010 November;57(11):2564–2571.

10. Gong S, Piazza G. Design and analysis of lithium–niobate-based high electromechanical coupling RF-MEMS resonators for wideband filtering. IEEE Transactions on Microwave Theory and Techniques. 2013 Jan;61(1):403–414.

11. Wang R, Bhave SA, Bhattacharjee K. Design and fabrication of S_0 lamb-wave thin-film lithium niobate micromechanical resonators. Journal of Microelectromechanical Systems. 2015 April;24(2):300–308.

12. Olsson RH III, Hatter K, Homeijer SJ, Wiwi M, Eichenfield M, Branch DW. A high electromechanical coupling coefficient SH0 lamb wave lithium niobate micromechanical resonator and a method for fabrication. Sensors and Actuators A. 2014;209:183–190.

13. Pulskamp JS, Rudy RQ, Bedair SS, Puder JM, Polcawich RG. Ferroelectric PZT MEMS HF/VHF resonators/filters. Proc IEEE Int Freq Control Symp. (IFCS); 2016; New Orleans, LA. p. 1–4.

14. Wasa K, Matsushima T, Adachi H, Matsunaga T, Suzuki M, Yanagitani T, Yamamoto T, Yoshida S, Tanaka S, Trolier-McKinstry S. PZT-based high coupling with low permittivity thin films. 2013 Joint IEEE International Symposium on Applications of Ferroelectric and Workshop on Piezoresponse Force Microscopy (ISAF/PFM); 2013; Prague, Czech Republic. p. 69–72.

15. Trolier-McKinstry S, Muralt P. Thin film piezoelectrics for MEMS. J. Electroceramics. 2004;12:7–17.

16. Pulskamp JS, Bedair SS, Polcawich RG, Judy D, Bhave SA. Ferroelectric PZT RF MEMS resonators. 2011 Joint Conference of the IEEE International Frequency Control and the European Frequency and Time Forum (FCS) Proceedings; 2011; San Francisco, CA. p. 1–6.

17. Bedair SS, Pulskamp JS, Polcawich RG, Judy D, Gillon A, Bhave S, Morgan B. Low loss micromachined lead zirconate titanate, contour mode resonator with 50Ω termination. Micro Electro Mechanical Systems (MEMS), 2012 IEEE 25th International Conference on; 2012; Paris, France. p. 708–712.

18. Ho GK, Abdolvand R, Sivapurapu A, Humad S, Ayazi F. Piezoelectric-on-silicon lateral bulk acoustic wave micromechanical resonators. J Microelectromech Syst. 2008 Apr;17(2):512–520.

19. DeVoe DL. Piezoelectric thin film micromechanical beam resonators. Sensors and Actuators A. 2001 Jan;88(3):263–272.

20. Dick AJ, Balachandran B, DeVoe DL, Mote CD Jr. Parametric identification of piezoelectric microscale resonators. Journal of Micrmechanics and Microengineering. 2006 Jan;16(8):1593–1601.

21. Pulskamp JS, Bedair SS, Polcawich RG, Smith GL, Martin J, Power B, Bhave SA. Electrode-shaping for the excitation and detection of permitted arbitrary modes in arbitrary geometries in piezoelectric resonators. Ultrasonics, Ferroelectrics, and Frequency Control, IEEE Transactions on. 2012 May;59(5):1043–1060.

22. Rudy RQ, Pulskamp JS, Bedair SS, Puder JM, Polcawich RG. Piezoelectric disk flexure resonator with 1 dB loss. Proc IEEE Int Freq Control Symp. (IFCS); 2016; New Orleans, LA. p. 1–4.

23. Puder JM, Pulskamp JS, Rudy RQ, Polcawich RG, Bhave SA. Fundamental limits of disk flexure resonators. 2017 Joint Conference of the European Frequency and Time Forum and IEEE International Frequency Control Symposium (EFTF/IFCS); 2017; Besancon, France. p. 558–560.

24. Potrepka DM, Fox GR, Sanchez LM, Polcawich RG. Pt/TiO2 growth templates for enhanced PZT films and MEMS devices. MRS Proceedings. 2011;1299.

25. Sanchez LM, Potrepka DM, Fox GR, Takeuchi I, Wang K, Bendersky LA, Polcawich RG. Optimization of PbTiO3 seed layers and Pt metallization for PZT-based piezoMEMS actuators. Journal of Materials Research. 2013;28(14):1920–1931.

26. Larson JD III, Bradley RC, Wartenberg S, Ruby RC. Modified Butterworth-Van Dyke circuit for FBAR resonators and automated measurement system. Ultrasonics Symposium, 2000 IEEE. 2000 Oct;1:863–868.

27. Kajfez D. Q-Factor. In: Chang K, editor. Encyclopedia of RF and Microwave Engineering. New York (NY): Wiley; 2005.

28. Cassella C, Hui Y, Qian Z, Hummel G, Rinaldi M. Aluminum nitride cross-sectional lamé mode resonators. Journal of Microelectromechanical Systems. 2016 April;25(2):275–285.

29. Puder JM, Bedair SS, Pulskamp JS, Rudy RQ, Polcawich RG, Bhave SA. Higher dimensional flexure mode for enhanced effective electromechanical coupling in PZT-on-silicon MEMS resonators. Solid-State Sensors, Actuators and Microsystems (TRANSDUCERS), 2015 Transducers – 2015 18th International Conference on; 2015; Anchorage, AK. p. 2017–2020.

30. Gabrielson T. Frequency constants for transverse vibration of annular disks. Journal of the Acoustical Society of America. 1999 Jun;105(6):3311–3317.

31. Bedair SS, Pulskamp JS, Polcawich RG, Rudy RQ, Puder J. Thin-film piezoelectric transformers operating in harmonics of out-of-plane flexure modes. Solid-State Sensors, Actuators and Microsystems (TRANSDUCERS), 2015 Transducers - 2015 18th International Conference on; 2015; Anchorage, AK. p. 714–717.

32. Rudy RQ, Pulskamp JS, Bedair SS, Breen MG, Puder JM, Polcawich RG. Low-loss gold-laced PZT-on-silicon resonator with reduced parasitics. 2016 IEEE 29th International Conference on Micro Electro Mechanical Systems (MEMS); 2016; Shanghai. p. 675–678.

33. Zuo C, Shin N, Piazza G. Very high frequency channel-select MEMS filters based on self-coupled piezoelectric AlN contour-mode resonators. Sensors and Actuators A. 2010;160(1–2):132–140.

34. Digi-Key Electronics. RF filters. c2018 [accessed 2018 Aug 29]. https://www.digikey.com/products/en/filters/rf-filters/844.

35. Segovia-Fernandez J, Cremonesi M, Cassella C, Frangi A, Piazza G. Anchor losses in AlN contour mode resonators. Journal of Microelectromechanical Systems. 2015 April;24(2):265–275.

36. Tabrizian R, Rais-Zadeh M. The effect of charge redistribution on limiting the kt^2Q product of piezoelectrically transduced resonators. 2015 Transducers - 2015 18th International Conference on Solid-State Sensors, Actuators and Microsystems (TRANSDUCERS); 2015; Anchorage, AK. p. 981–984.

List of Symbols, Abbreviations, and Acronyms

AIN	aluminum nitride
ALD	atomic layer deposition
BVD	Butterworth Van Dyke
FOM	figure of merit
HF	high frequency
LN	lithium niobate
mBVD	modified Butterworth Van Dyke
MEMS	microelectromechanical system
PZT	lead zirconate titanate
RF	radio frequency
SAW	surface acoustic wave
SOI	silicon-on-insulator
VHF	very high frequency
ZnO	zinc oxide

1 (PDF) DEFENSE TECHNICAL INFORMATION CTR DTIC OCA

2 (PDF) DIR ARL
IMAL HRA
RECORDS MGMT
RDRL DCL
TECH LIB

1 (PDF) GOVT PRINTG OFC
A MALHOTRA

1 (PDF) ARL
RDRL SER L
RQ RUDY